



Topology optimization driven by anisotropic mesh adaptation: Towards a free-form design



Stefano Micheletti ^{a,*}, Simona Perotto ^a, Luca Soli ^b

^aMOX, Dipartimento di Matematica, Politecnico di Milano, Piazza Leonardo da Vinci 32, I-20133 Milano, Italy

^bThales Alenia Space S.p.A. Italia, Via E. Mattei 1, I-20064 Gorgonzola, MI, Italy

ARTICLE INFO

Article history:

Received 16 July 2018

Accepted 17 January 2019

Available online 2 February 2019

Keywords:

Topology optimization

Anisotropic adapted meshes

Recovery-based error estimators

Free-form design

ABSTRACT

We propose the new adaptive algorithm SIMPATY for topology optimization to design lightweight and stiff structures exhibiting free-form features. This is achieved by properly combining the classical SIMP method with an anisotropic mesh adaptation strategy based on a recovery-based a posteriori error estimator. Mesh adaptivity allows us to contain (and, for simple structures, even to eliminate) the filtering usually adopted in a topology optimization context. Thus, the final layout is intrinsically smooth, so that the post-processing phase can be strongly reduced (or even skipped), and the structure can directly move on to the production manufacturing phase. A free-form design is also enhanced by anisotropic mesh adaptivity. An extensive numerical validation supports these remarkable properties.

© 2019 Elsevier Ltd. All rights reserved.

1. Motivations

We are interested in the design of structures with lightweight properties combined with good resistance to applied loads. This issue is certainly of utmost relevance in different branches of industrial design, such as space, biomedical, mechanical, architecture (see, e.g., [1–5]). For example, in the space industry, due to the high cost of exploration missions, even a minimum save on the total mass of the spacecraft can reduce significantly the total launch cost, as the rocket and the satellite orbital maneuvers require less propellant. Topology optimization is the common mathematical tool to tackle the design problem, despite the obvious difference among these fields. In short, topology optimization seeks an optimal structure in a design domain for assigned loads and boundary conditions, under some constraints (see [6–10] and the references therein). For example, typical optimality criteria are minimum volume, minimum compliance (or maximum stiffness), maximum fundamental frequency in the dynamic case, while constraints can be maximum allowed displacements and stresses, or a given fraction of the initial volume. One of the well known mathematical formulations for topology optimization is the so-called SIMP (Solid Isotropic Material with Penalization) method [7,6,10]. This belongs to the family of density-based methods, where the problem unknown is a scalar field, referred to as density, taking values between zero (absence of material) and

one (presence of material). The final layout of the structure is obtained by extracting the parts of the domain where the density is one. In practice, intermediate values of the density have to be filtered out, and this is obtained through a suitable penalty exponent, which pushes the density towards either the value zero or one. Other approaches are possible, and the most important ones can be classified in: level-set methods [11,12], topological derivative procedures [13], phase field techniques [14,15], evolutionary approaches [16], homogenization [6,17], performance-based optimization [18].

Most of the works in the literature employ a discretization based on a fixed structured grid. This choice in turn is known to suffer from mesh dependency and checkerboard phenomena [7,19,20], which are contained to some extent by filtering techniques, which smooth out the density over small patches of elements [21,22].

A possible mitigation to mesh dependency and checkerboard effects is provided by mesh adaptation. In [23], a topology optimization algorithm with goal-oriented error control to drive mesh adaptivity is considered, relying on a standard ESTIMATE-MARK-REFINE iterative scheme on structured triangular grids, yet requiring filtering. Another approach is the one used, for example, in [24], where anisotropic mesh adaptation is carried out based on a heuristic approach. In particular, a combination of filtered continuous sensitivities and filtered design variables is employed to drive mesh adaptation.

The approach proposed in the present work consists of anisotropic mesh adaptation based on a theoretically sound tool, i.e., a

* Corresponding author.

E-mail address: stefano.micheletti@polimi.it (S. Micheletti).

recovery-based a posteriori error analysis. Namely, the estimator developed in [25–27] is applied in an original way to the density function of the SIMP method to drive mesh adaptation. The resulting procedure is the subject of a pending patent [28], where we set up the overall optimization-adaptive procedure in the algorithm SIMPATY (SIMP with AdaptiviT). This new algorithm enjoys several advantages: a correctly adapted mesh, even with no filter at all, allows us to move towards a free-form design, in a cost-effective procedure, and alleviates the end user from most of the post-processing step, since the density is intrinsically characterized by sharp and smooth gradients. Thus, it suffices to cut off the elements of the mesh where the density is below a given threshold, to extract the final layout in a handy and automatic way. This feature is in contrast to what is generally required by most of the standard algorithms, where a strong post-processing can be required before getting the final structure.

The layout of the paper is the following. In Section 2, we recall the formulation of the SIMP method, along with the first optimization algorithm on a fixed grid. Section 3 introduces the anisotropic setting, the recovery-based anisotropic a posteriori error estimator, and the SIMPATY algorithm, which is employed, along with some variants, in Section 4 on several benchmark test cases. The SIMPATY potential of delivering a free-form design is established in Section 5, where more complex geometries are considered, including a simplified bracket for satellite applications. Finally, in Section 6 we draw some conclusions and lay down some future scenarios.

2. Elements of topology optimization: the SIMP method

Given a loaded structure $\Omega \subset \mathbb{R}^2$, we aim at identifying the optimal topology which minimizes the compliance or, equivalently, maximizes the structure stiffness under a volume constraint. In particular, we assume the traction, $\mathbf{f} : \Gamma_N \rightarrow \mathbb{R}^2$, to be applied on a portion Γ_N of the body boundary $\partial\Omega$. The compliance is given by

$$\int_{\Gamma_N} \mathbf{f} \cdot \mathbf{u} d\gamma,$$

with $\mathbf{u} = (u_1, u_2)^T : \Omega \rightarrow \mathbb{R}^2$ the induced displacement field.

The mathematical model underlying the structure deformation is represented by the linear elasticity equation [29]

$$\begin{cases} -\nabla \cdot \sigma(\mathbf{u}) = \mathbf{0} & \text{in } \Omega \\ \mathbf{u} = \mathbf{0} & \text{on } \Gamma_D \\ \sigma(\mathbf{u})\mathbf{n} = \mathbf{f} & \text{on } \Gamma_N \\ \sigma(\mathbf{u})\mathbf{n} = \mathbf{0} & \text{on } \Gamma_F, \end{cases} \quad (1)$$

where $\sigma(\mathbf{u}) = 2\mu\varepsilon(\mathbf{u}) + \lambda\text{tr}(\varepsilon(\mathbf{u}))I$ denotes the stress tensor, with $\varepsilon(\mathbf{u}) = (\nabla\mathbf{u} + \nabla\mathbf{u}^T)/2$ the small displacement strain tensor,

$$\lambda = \frac{Ev}{(1+v)(1-2v)}, \quad \mu = \frac{E}{2(1+v)}$$

the Lamé coefficients, E is Young modulus, v is Poisson ratio, $\text{tr}(\cdot)$ is the trace operator, I the identity tensor, \mathbf{n} the unit outward normal vector to $\partial\Omega$, Γ_D is the portion of the boundary where the structure is clamped, and Γ_F is the traction-free boundary.

Model (1) represents the building block of the SIMP method [7,10]. This approach introduces a density function $\rho \in L^\infty(\Omega)$ taking values in $[0, 1]$, representing the distribution of the material in the structure. Throughout the paper, we adopt standard notation for function spaces [30]. Ideally, we expect only the extremal values, $\rho = 0$ (void) and $\rho = 1$ (material). Nevertheless, all the intermediate values are allowed and have to be penalized in the formulation. In particular, we adopt the standard power law penalization function ρ^p , with $p \geq \max\{2/(1-v), 4/(1+v)\}$ [7].

Function ρ^p penalizes intermediate values by promoting essentially the values of ρ close to one, which correspond to the stiffest material, consistently with the minimization of the compliance. Consequently, the SIMP approach entails solving model (1) with a modified Hooke law, which replaces λ with $\rho^p\lambda$ and μ with $\rho^p\mu$. With a view to the optimization problem, we first provide the weak form of the modified linear elasticity equation: find

$$\mathbf{u} \in U = \left\{ \mathbf{v} \in [H^1(\Omega)]^2 : \mathbf{v} = \mathbf{0} \text{ on } \Gamma_D \right\} \text{ such that} \\ a(\mathbf{u}, \mathbf{v}) = \mathcal{C}(\mathbf{v}) \quad \forall \mathbf{v} \in U, \quad (2)$$

with

$$a(\mathbf{u}, \mathbf{v}) = \int_{\Omega} \sigma_\rho(\mathbf{u}) : \varepsilon(\mathbf{v}) d\mathbf{x}, \quad \mathcal{C}(\mathbf{v}) = \int_{\Gamma_N} \mathbf{f} \cdot \mathbf{v} d\gamma,$$

and $\sigma_\rho(\mathbf{u}) = \rho^p[2\mu\varepsilon(\mathbf{u}) + \lambda\text{tr}(\varepsilon(\mathbf{u}))I]$. Notice that $\mathcal{C}(\mathbf{u}) = a(\mathbf{u}, \mathbf{u})$ coincides with the compliance to be minimized.

The full SIMP method thus reads: find ρ such that

$$\min_{\rho \in L^\infty(\Omega)} \mathcal{C}(\mathbf{u}(\rho)) : \begin{cases} a(\mathbf{u}(\rho), \mathbf{v}) = \mathcal{C}(\mathbf{v}) \quad \forall \mathbf{v} \in U \\ \int_{\Omega} \rho d\mathbf{x} \leq \alpha|\Omega| \\ \rho_{\min} \leq \rho \leq 1, \end{cases} \quad (3)$$

where $0 < \alpha < 1$ denotes the maximum allowable volume fraction, with respect to the original volume $|\Omega|$, and $0 < \rho_{\min} < 1$ is a lower bound for the density, which ensures the elasticity system to be well-defined. We observe that (3) generally exhibits multiple local minima, due to the non-convexity of the problem. This is the reason why one cannot a priori guarantee the uniqueness of the solution [7].

Problem (3) is numerically tackled via a finite element discretization [31]. We introduce a conforming tessellation $\mathcal{T}_h = \{K\}$ of $\bar{\Omega}$, with K a generic triangular tile. We denote by V_h^d the associated finite element space of (piecewise continuous polynomials of) degree d , with the understanding that for $d = 0$ the functions are discontinuous and piecewise constant on \mathcal{T}_h . The discrete counterpart of (3) thus reads: find ρ_h such that

$$\min_{\rho_h \in V_h^d} \mathcal{C}(\mathbf{u}_h(\rho_h)) : \begin{cases} a(\mathbf{u}_h(\rho_h), \mathbf{v}_h) = \mathcal{C}(\mathbf{v}_h) \quad \forall \mathbf{v}_h \in [V_h^s]^2 \cap U \\ \int_{\Omega} \rho_h d\mathbf{x} \leq \alpha|\Omega| \\ \rho_{\min} \leq \rho_h \leq 1, \end{cases} \quad (4)$$

with $\mathbf{u}_h(\rho_h) \in [V_h^s]^2 \cap U$.

The SIMP is known to suffer from two main drawbacks, the dependency on the selected mesh and the presence of checkerboards [20,7]. The former issue arises when the numerical solution to the optimization problem depends on the mesh at hand, due to the non-uniqueness issue. The latter issue is related to discretization and leads to alternating solid and void elements in a checkerboard pattern. This is due to the two-field formulation, involving density and displacement. Certain combinations of finite elements turn out to be unstable, similarly to the two-field pressure-velocity formulation of the Stokes problem.

Possible remedies to mesh dependency consist of adding explicit limitations on the allowable density distributions or of filtering the density. This may be useful also to contain checkerboard effects. The employment of higher order finite elements for the displacement with respect to the density ($s \geq r$ in (4)) is an alternative viable method to avoid the checkerboard problem. Higher order finite elements, however, require high CPU times, even though they remain affordable in two dimensions. The non-uniqueness of the solution remains an issue, independently of the selected discretization.

Concerning the specific choice made in SIMPATY algorithm for s and r , we choose $s = r = 1$, since we rely on a beneficial effect of anisotropic mesh adaptation with no filter at all. When we switch off mesh adaptation, we resort to a low-pass filter based on the

diffusion kernel, namely, we replace the discrete density ρ_h with its filtered version, ρ_f , which solves the following Helmholtz-type partial differential problem

$$\begin{cases} -\tau^2 \Delta \rho_f + \rho_f = \rho_h & \text{in } \Omega \\ \tau^2 \nabla \rho_f \cdot \mathbf{n} = 0 & \text{on } \partial\Omega, \end{cases} \quad (5)$$

with τ a real parameter measuring the thickness of the smoothed density, to be properly tuned [21].

The algorithm merging the SIMP method with the Helmholtz filter is provided in

Algorithm 1. SIMP algorithm on a fixed grid

```

Input: TOL, kmax,  $\rho_{\min}$ ,  $\alpha$ 
Set:  $\rho_h^0 \leftarrow 1$ , k  $\leftarrow 0$ , err  $\leftarrow 1 + \text{TOL}$ 
while (err > TOL & k < kmax) then
  1.  $\rho_h^{k+1} \leftarrow \text{IPOPT}(\rho_h^k, \rho_{\min}, \text{Mit} = 10, \alpha, \dots)$ ;
  2.  $\rho_h^{k+1} \leftarrow \rho_f(\rho_h^{k+1})$ ;
  3. err  $\leftarrow \|\rho_h^{k+1} - \rho_h^k\|_\infty$ ;
  4. k  $\leftarrow k + 1$ ;
end

```

end

Some comments are in order. In line 1, the optimization problem (4) is solved via the Interior Point OPTimizer (IPOPT) package [32]. IPOPT is a common large-scale nonlinear optimization tool based on the interior point algorithm [33]. Both equality and inequality constraints can be tackled via suitable slack variables. Constraints may involve both the control variable (for example, the density) as well as functions of the control variable (for example, the total volume of the structure). We have highlighted only the main input parameters, i.e., the initial guess, ρ_h^k , the minimum density, ρ_{\min} , the maximum number of iterations, Mit, and the maximum volume fraction, α . The tolerance for the stopping criterion is always understood to be set to 10^{-6} .

Among the input parameters of IPOPT, the computation of the gradient of the compliance with respect to the density, $\nabla_\rho \mathcal{C}$, needs more details. With this aim, we resort to the Lagrangian functional

$$\mathcal{L} = \mathcal{L}(\mathbf{u}, \mathbf{z}, \rho) = \mathcal{C}(\mathbf{u}) + a(\mathbf{u}, \mathbf{z}) - \mathcal{C}(\mathbf{z}),$$

where $\mathbf{z} \in U$ is the Lagrange multiplier. It is well known that

$$\nabla_\rho \mathcal{C}(\rho) = \nabla_\rho \mathcal{L}|_{\{\mathbf{u}(\rho), \mathbf{z}(\rho), \rho\}},$$

where $\mathbf{u}(\rho)$ and $\mathbf{z}(\rho)$ are the solutions to the primal and the adjoint problem associated with the Gâteaux derivative of \mathcal{L} with respect to \mathbf{z} and \mathbf{u} , respectively. In particular, the primal problem coincides with (2), whereas the adjoint problem reads: find $\mathbf{z} \in U$ such that

$$a(\mathbf{v}, \mathbf{z}) = -\mathcal{C}(\mathbf{v}) \quad \forall \mathbf{v} \in U. \quad (6)$$

On comparing (6) with (2) and due to the self-adjointness of $a(\cdot, \cdot)$, we infer that $\mathbf{z} = -\mathbf{u}$, i.e., the adjoint solution is for free. Finally, the Gâteaux derivative of \mathcal{L} with respect to ρ along the direction φ is

$$\langle \nabla_\rho \mathcal{C}, \varphi \rangle = \int_{\Omega} p \rho^{p-1} \sigma(\mathbf{u}) : \varepsilon(\mathbf{z}) \varphi d\mathbf{x},$$

which implies $\nabla_\rho \mathcal{C}(\rho) = -p \rho^{p-1} \sigma(\mathbf{u}(\rho)) : \varepsilon(\mathbf{u}(\rho))$. Thus, each evaluation of the gradient of the compliance requires only a primal solve. In more detail, on the discrete level, the i -th component of the gradient vector is provided by

$$[\nabla_{\rho_h} \mathcal{C}(\rho_h)]_i = \langle \nabla_{\rho_h} \mathcal{C}, \varphi_{h,i} \rangle = - \int_{\Omega} p \rho_h^{p-1} \sigma(\mathbf{u}_h) : \varepsilon(\mathbf{u}_h) \varphi_{h,i} d\mathbf{x},$$

where $\{\varphi_{h,i}\}_i$ represents the finite element basis of the space V_h^r .

The output density, ρ_h^{k+1} , from IPOPT is then filtered in line 2, by approximating (5) via linear finite elements.

The global convergence check in line 3, is based on the stagnation of the density function between successive iterations to within a user-defined tolerance TOL and a maximum number kmax of iterations.

2.1. The basic test case

We assess the performance of **Algorithm 1** on the standard cantilever test case whose geometry and setting are sketched in Fig. 1.

The design domain is $\Omega = (0, 3) \times (0, 1)$. The elastic model (1) is characterized by the data $\mathbf{f} = (0, -80)^T$, $\Gamma_D = \{(x, y) : x = 0, 0 \leq y \leq 1\}$, $\Gamma_N = \{(x, y) : x = 3, 0.45 \leq y \leq 0.55\}$, $\Gamma_F = \partial\Omega \setminus (\Gamma_D \cup \Gamma_N)$, $E = 10^3$, $v = 1/3$. The SIMP exponent p is set to 3, the mesh \mathcal{T}_h is structured and consists of 9600 regular elements and we employ linear finite elements for both density and displacement. The parameter of the Helmholtz filter is set to $\tau = 0.02$. Concerning the parameters for **Algorithm 1**, we choose $\text{TOL} = 8 \cdot 10^{-2}$, $\text{kmax} = 100$, $\rho_{\min} = 0.01$ and $\alpha = 0.5$.

The algorithm stops after 39 iterations. Fig. 2, top, shows the output density of **Algorithm 1**. The output structure is the standard one in the literature (see, e.g., [7] for the same aspect ratio of the geometry). Fig. 2, bottom, furnishes the output obtained with a variant of **Algorithm 1**, where we fix $\text{kmax} = 1$, we increase the number Mit of the IPOPT iterations to 100 to allow the full convergence of the optimization algorithm and we skip the filtering phase. As expected, the predicted structure is very rough, even though it identifies the same topology as in the previous run.

Fig. 3 highlights the benefits of filtering and of a shrewd choice of the finite element pair (ρ_h, \mathbf{u}_h) . In the first row, we choose

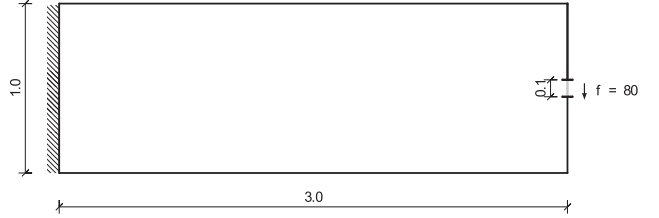


Fig. 1. Cantilever test case: geometry and load.

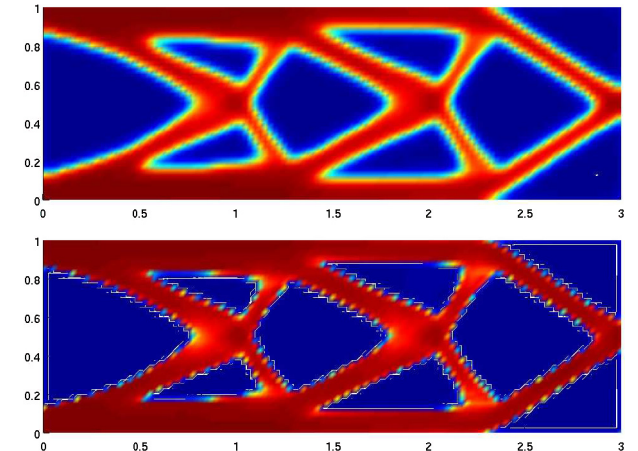


Fig. 2. Cantilever test case: optimal density with (top) and without (bottom) filtering.

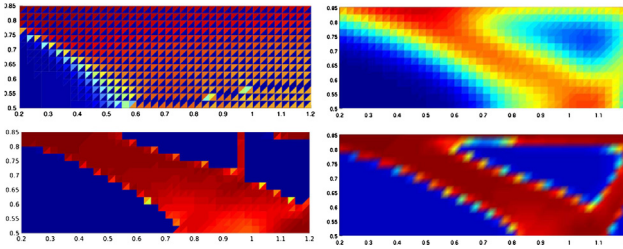


Fig. 3. Cantilever test case: effect of the filter and of the degree of the finite element approximation (the same colormap is used in all panels).

$r = 0, s = 1$, and we switch off (left) and on (right) the Helmholtz-type filter. It is evident that the action of the filter alleviates the checkerboard pattern. Notice that, for a piecewise constant ρ_h , the filtered density (piecewise linear) is mapped to the \mathbb{P}_0 finite element space in line 2 of [Algorithm 1](#) by local L^2 -projection.

In the second row, we do not apply the filter and we change the discrete space for the density, fixing $s = 2$. In particular, we pick $r = 0$ (left) and $r = 1$ (right). In both cases, no checkerboard appears. For the choice $r = 0$, some very thin struts (not desirable for printing) are generated. A jagged boundary is present in both cases, due to the employment of a not sufficiently fine or adapted mesh.

3. An anisotropic variant of the SIMP method

The reference anisotropic background is the one exploited, e.g., in [\[34,35\]](#). The anisotropic properties of a generic triangle K of the mesh $\mathcal{T}_h = \{K\}$ are extracted out of the spectral properties of the standard affine map T_K between the equilateral reference element \hat{K} inscribed in the unit circle and K , i.e.,

$$\mathbf{x} = T_K(\hat{\mathbf{x}}) = M_K \hat{\mathbf{x}} + \mathbf{t}_K,$$

with $\mathbf{x} \in K, \hat{\mathbf{x}} \in \hat{K}, M_K \in \mathbb{R}^{2 \times 2}, \mathbf{t}_K \in \mathbb{R}^2$. In particular, we factorize the Jacobian M_K through the polar decomposition $M_K = B_K Z_K$, with $B_K \in \mathbb{R}^{2 \times 2}$ a symmetric positive definite matrix stretching the triangle K , and $Z_K \in \mathbb{R}^{2 \times 2}$ an orthogonal matrix which rotates K . Then, we introduce the classical eigenvalue-eigenvector factorization of B_K as $B_K = R_K^T \Lambda_K R_K$, with $R_K^T = [\mathbf{r}_{1,K}, \mathbf{r}_{2,K}]$ and $\Lambda_K = \text{diag}(\lambda_{1,K}, \lambda_{2,K})$, with $\lambda_{1,K} \geq \lambda_{2,K} > 0$. The eigenvectors $\mathbf{r}_{1,K}, \mathbf{r}_{2,K}$ identify the directions of the semi-axes of the ellipse circumscribed to K , while the eigenvalues $\lambda_{1,K}, \lambda_{2,K}$ measure the length of these semi-axes (see [\[34,35\]](#) for more details). A measure of the anisotropic deformation is provided by the aspect ratio of the element K , $s_K = \lambda_{1,K}/\lambda_{2,K} \geq 1$: the higher s_K , the larger the deviation from the equilateral shape, for which $s_K = 1$.

3.1. The recovery-based error estimator

A standard recovery-based adaptive procedure consists of two steps, i.e., the proposal of a recovered gradient based on the discrete solution, and its employment to estimate the $H^1(\Omega)$ -seminorm of the discretization error [\[36–38\]](#). In [\[25–27\]](#), an extension of this procedure to the anisotropic context has been proposed. With a view to the anisotropic analysis, we have introduced a new recipe for the recovered gradient, $P(\nabla u_h)$. The main difference with respect to [\[37\]](#) is that $P(\nabla u_h)$ is piecewise constant over the patches $\Delta_K = \{T \in \mathcal{T}_h : T \cap K \neq \emptyset\}$, instead of being piecewise linear continuous on Ω . In particular, the patchwise restriction of $P(\nabla u_h)$ coincides with the area-weighted average over the patch Δ_K of the gradient of the discrete solution, namely,

$$P(\nabla u_h)|_{\Delta_K} = \frac{1}{|\Delta_K|} \sum_{T \in \Delta_K} |T| \nabla u_h|_T,$$

with $u_h \in V_h^1$. Thus, the associated a posteriori anisotropic error estimator is

$$\eta^2 = \sum_{K \in \mathcal{T}_h} \eta_K^2. \quad (7)$$

whose local contribution is defined by

$$\eta_K^2 = \frac{1}{\lambda_{1,K} \lambda_{2,K}} \sum_{i=1}^2 \lambda_{i,K}^2 \left(\mathbf{r}_{i,K}^T G_{\Delta_K}(E_{\nabla}) \mathbf{r}_{i,K} \right), \quad (8)$$

with $E_{\nabla} = [P(\nabla u_h) - \nabla u_h]|_{\Delta_K}$ the recovered error, and where $G_{\Delta_K}(\cdot) \in \mathbb{R}^{2 \times 2}$ is the symmetric semidefinite positive matrix with entries

$$[G_{\Delta_K}(\mathbf{w})]_{ij} = \sum_{T \in \Delta_K} \int_T w_i w_j d\mathbf{x} \quad \text{with } i, j = 1, 2, \quad (9)$$

for any vector-valued function $\mathbf{w} = (w_1, w_2)^T \in [L^2(\Omega)]^2$. The scaling factor $(\lambda_{1,K} \lambda_{2,K})^{-1}$ in [\(8\)](#) ensures consistency with the isotropic case ($\lambda_{1,K} = \lambda_{2,K}$).

Estimator [\(7\)](#) and [\(8\)](#) is inspired by the anisotropic interpolation error estimate provided in [\[39\]](#) for a quasi-interpolant operator I_h ,

$$\|v - I_h(v)\|_{L^2(K)} \leq C \left(\sum_{i=1}^2 \lambda_{i,K}^2 \left(\mathbf{r}_{i,K}^T G_{\Delta_K}(\nabla v) \mathbf{r}_{i,K} \right) \right)^{1/2},$$

with C a constant depending on the shape regularity of the patch Δ_K and for any $v \in H^1(\Omega)$.

3.2. The adaptive SIMP algorithm

We resort to a metric-based approach to generate the new adapted mesh by exploiting the information provided by η .

A metric, $\mathcal{M} : \Omega \rightarrow \mathbb{R}^{2 \times 2}$, is a symmetric positive definite tensor field which contains all the geometric information related to a certain mesh [\[40\]](#). In practice, we will approximate \mathcal{M} with a piecewise constant function, $\mathcal{M}_{\mathcal{T}_h}$, associated with the actual grid \mathcal{T}_h , such that $\mathcal{M}_{\mathcal{T}_h}|_K = R_K^T \Lambda_K^{-2} R_K$, using the local estimator η_K in a predictive way. This goal is reached via an iterative procedure, which eventually yields an optimal adapted grid, i.e., the mesh minimizing the number of elements under the constraint $\eta \leq \text{MTOL}$ on the accuracy, with MTOL a tolerance fixed by the user. The tricky step is the prediction of the metric $\mathcal{M}_{\mathcal{T}_h}$ from the estimator. We outline here the procedure adopted for this purpose, while referring to, e.g., [\[35,34,41,26\]](#) for more details.

With reference to the generic iteration of the adaptive procedure, we rewrite estimator η_K by collecting the size information of the element in a unique factor, as

$$\eta_K^2 = \lambda_{1,K} \lambda_{2,K} |\hat{\Delta}_K| \left[S_K \left(\mathbf{r}_{1,K}^T \hat{G}_{\Delta_K}(E_{\nabla}) \mathbf{r}_{1,K} \right) + S_K^{-1} \left(\mathbf{r}_{2,K}^T \hat{G}_{\Delta_K}(E_{\nabla}) \mathbf{r}_{2,K} \right) \right],$$

where $\hat{G}_{\Delta_K}(\cdot)$ is the scaled matrix $G_{\Delta_K}(\cdot)/|\Delta_K|$, and $|\Delta_K| = \lambda_{1,K} \lambda_{2,K} |\hat{\Delta}_K|$, with $\hat{\Delta}_K = T_K^{-1}(\Delta_K)$. The area-dependent quantity is $\lambda_{1,K} \lambda_{2,K} |\hat{\Delta}_K|$, while the remaining term depends on orientation ($\mathbf{r}_{i,K}, i = 1, 2$) and aspect ratio (S_K). Minimizing the cardinality of the mesh implies maximizing the size of the element, i.e., minimizing the quantity

$$\mathcal{J}(S_K, \{\mathbf{r}_{i,K}\}_{i=1,2}) = S_K \left(\mathbf{r}_{1,K}^T \hat{G}_{\Delta_K}(E_{\nabla}) \mathbf{r}_{1,K} \right) + S_K^{-1} \left(\mathbf{r}_{2,K}^T \hat{G}_{\Delta_K}(E_{\nabla}) \mathbf{r}_{2,K} \right),$$

where it is understood that matrix $\hat{G}_{\Delta_K}(E_{\nabla})$ is known and computed using information on the current mesh and discrete solution. Thus, we are led to solve the constrained minimization problem

$$\min_{s_K, \mathbf{r}_{i,K}} \mathcal{J}(s_K, \{\mathbf{r}_{i,K}\}_{i=1,2}) : \begin{cases} \mathbf{r}_{i,K} \cdot \mathbf{r}_{j,K} = \delta_{ij} \\ s_K \geq 1, \end{cases} \quad (10)$$

with δ_{ij} the Kronecker symbol. The solution to this problem is provided by the following result (see [42] for the proof).

Proposition 3.1. Let $\{g_i, \mathbf{g}_i\}_{i=1,2}$ be the eigen-pairs associated with $\widehat{G}_{\Delta_K}(E_{\nabla})$, with $g_1 \geq g_2 > 0$ and $\{\mathbf{g}_i\}_{i=1,2}$ orthonormal. Then, $\mathcal{J}(\cdot)$ is minimized when $s_K = s_K^*$, $\mathbf{r}_{i,K} = \mathbf{r}_{i,K}^*$, with

$$s_K^* = \sqrt{g_1/g_2}, \quad \mathbf{r}_{1,K}^* = \mathbf{g}_2, \quad \mathbf{r}_{2,K}^* = \mathbf{g}_1. \quad (11)$$

The optimal metric associated with K is identified by $\mathbf{r}_{1,K}^*$ and $\mathbf{r}_{2,K}^*$ in (11), while $\lambda_{1,K}^*$ and $\lambda_{2,K}^*$ are computed by combining the optimal s_K^* in (11) with the equidistribution criterion $\eta_K^2 = \text{MTOL}^2 / \#\mathcal{T}_h$, $\#\mathcal{T}_h$ being the mesh element cardinality. We obtain

$$\lambda_{1,K}^* = g_2^{-1/2} \left(\frac{\text{MTOL}^2}{2 \#\mathcal{T}_h |\widehat{\Delta}_K|} \right)^{1/2}, \quad \lambda_{2,K}^* = g_1^{-1/2} \left(\frac{\text{MTOL}^2}{2 \#\mathcal{T}_h |\widehat{\Delta}_K|} \right)^{1/2}. \quad (12)$$

The optimal piecewise constant metric $\mathcal{M}_{\mathcal{T}_h}$ is thus obtained simply by collecting the optimal values $\{\mathbf{r}_{i,K}^*\}_{i=1}^2$ and $\{\lambda_{i,K}^*\}_{i=1}^2$, for each $K \in \mathcal{T}_h$. The new metric is finally provided to the function `adaptmesh` in FreeFem++ [43] to generate the new adapted mesh.

Next step is to enrich the SIMP method with the anisotropic mesh adaptation. Since the density function solution to (4) exhibits very strong gradients across the material-void interface, we expect that an anisotropic mesh adaptation should be the ideal technique to sharply capture these directional features. The additional benefit of anisotropic mesh adaptivity is the possibility of avoiding any filtering procedure since the final structure is intrinsically smooth. This is very important for practical applications since the post-processing phase can be skipped and the structure can directly move on to the production phase.

The resulting modified SIMP algorithm is listed in

Algorithm 2. SIMPATY: SIMP with AdaptivIY

Input: CTOL, MTOL, kmax, ρ_{\min} , $\mathcal{T}_h^{(0)}$, α
Set: $\rho_h^0 \leftarrow 1$, $k \leftarrow 0$, errC $\leftarrow 1 + \text{CTOL}$
while (errC > CTOL & $k < \text{kmax}$) then
1. $\rho_h^{k+1} \leftarrow \text{IPOPT}(\rho_h^k, \rho_{\min}, \text{Mit} = \text{nk}, \alpha, \dots);$
2. $\mathcal{T}_h^{(k+1)} \leftarrow \text{adapt}(\mathcal{T}_h^{(k)}, \rho_h^{k+1}, \text{MTOL}, \text{method});$
3. $\text{errC} \leftarrow |\#\mathcal{T}_h^{(k+1)} - \#\mathcal{T}_h^{(k)}| / \#\mathcal{T}_h^{(k)};$
4. $k \leftarrow k + 1;$
end

The main difference with respect to Algorithm 1 is step 2., where mesh adaptation is carried out. Starting from the initial mesh $\mathcal{T}_h^{(0)}$, the SIMPATY algorithm generates a sequence of adapted meshes, $\{\mathcal{T}_h^{(k)}\}_k$, with associated densities $\{\rho_h^k\}_k$. Function `adapt` covers two adaptive strategies, i.e., the standard Hessian-based approach implemented in the built-in FreeFem++ function `adaptmesh` (`method = "AM"`), and the metric-based procedure based on the ZZ anisotropic error estimator (7) and (8) (`method = "ZZ"`). At step 3. we check the stagnation of the adapted mesh through the relative variation of the cardinality $\#\mathcal{T}_h$ of the mesh elements to within CTOL and a maximum number kmax of iterations.

The parameter nk is set to a moderate value (e.g., 10) at every iteration, except for the first one where it takes a larger value (e.g., 200). This choice should allow IPOPT to get very close to the optimal solution on the initial mesh, whereas a less strict check is expected to suffice in the next iterations. Essentially, we strike a balance between quality of the solution and non-optimality of the mesh. Indeed, it is not reasonable to compute an accurate density function on a rough intermediate mesh which is not necessarily the optimal one.

4. Standard benchmarks for SIMPATY algorithm

We focus on the very popular structure in the topology optimization community, i.e., the cantilever in Section 2.1, to check the effectiveness of Algorithm 2. This is to be considered as a preliminary assessment with a view to more challenging configurations.

4.1. Central Load Cantilever (CLC)

We apply the SIMPATY algorithm with the following values for the input parameters: $\text{CTOL} = 10^{-2}$, $\text{MTOL} = 0.5$, $\text{kmax} = 30$, $\rho_{\min} = 10^{-2}$, the initial mesh $\mathcal{T}_h^{(0)}$ is a 60×20 structured mesh and $\alpha = 0.5$. The SIMP parameter is $p = 3$, and nk is set as suggested above.

SIMPATY converges after 18 iterations. The corresponding density and mesh are shown in Fig. 4, first and second row, respectively. In particular, this mesh is obtained by a truncation procedure which preserves only the elements of the final adapted mesh $\mathcal{T}_h^{(18)}$, where the piecewise constant $L^2(\Omega)$ -projection of ρ_h^{18} is greater than or equal to the threshold value 0.5. The predicted structure is essentially the same as the one provided without adaptivity (see Fig. 2). Despite the absence of any filter and of any post-processing of the final mesh, we obtain an extremely smooth structure as it is evident on comparing the densities in Fig. 2, bottom, and Fig. 4, first row. Moreover, the density in Fig. 2, top, is less sharp compared with Fig. 4, first row, as highlighted by the presence of intermediate densities between matter and void. The anisotropic features of the mesh are particularly evident along the material-void interface where the gradient of the density is stronger. The outer horizontal sides make an exception since they coincide with a portion of the boundary of the original design domain. The maximum value attained for the aspect ratio is 203.07. The compliance directly computed solving system (1) on the truncated mesh is equal to 8.852.

For the sake of assessment, we carry out a comparison with three other adaptation techniques.

First, we run the isotropic version of SIMPATY algorithm, obtained by solving the optimization problem (10) with the constraint $s_K = 1$. The result is that

$$\lambda_{1,K}^* = \lambda_{2,K}^* = \left(\frac{g_1 + g_2}{2} \right)^{-1/2} \left(\frac{\text{MTOL}^2}{2 \#\mathcal{T}_h |\widehat{\Delta}_K|} \right)^{1/2},$$

which amounts to replacing both g_1 and g_2 in (12) by their arithmetic mean, $(g_1 + g_2)/2$, ensuring the same global accuracy MTOL. Fig. 4, third row, displays the corresponding truncated mesh. The number of elements is 29,497 to be compared with 4992 triangles of the anisotropic grid.

In Fig. 4, fourth row, we provide the anisotropic adapted mesh obtained by setting `method = "AM"` in SIMPATY. This function controls the interpolation error within a certain tolerance, here set to 0.25 to guarantee a number of elements comparable with the one in Fig. 4, second row. The anisotropy of this mesh is weaker

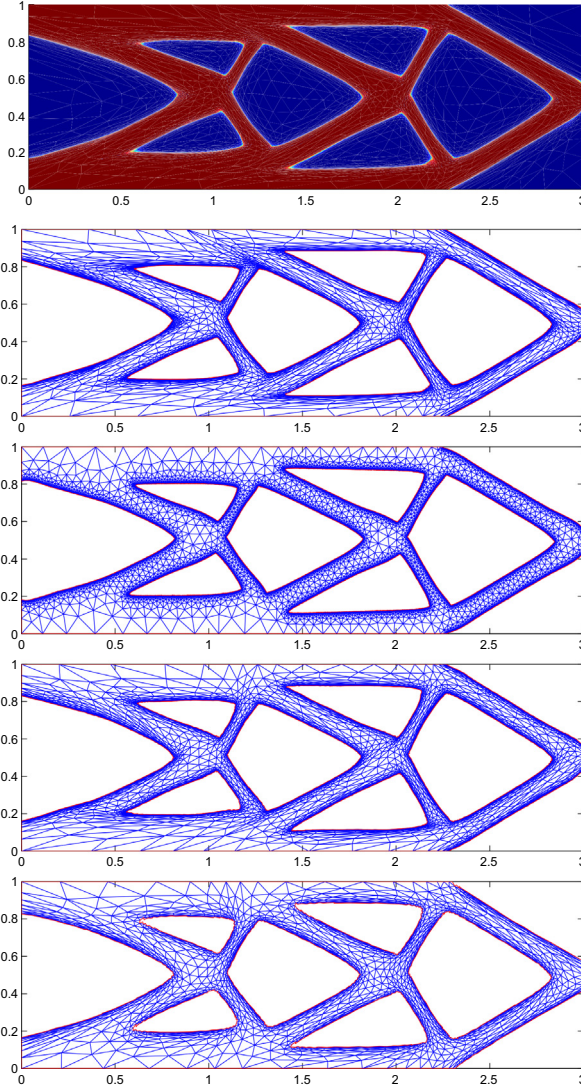


Fig. 4. CLC test case: optimal density (first row) and adapted mesh (second row) obtained with the anisotropic ZZ estimator; mesh generated via the isotropic ZZ estimator (third row), via adaptmesh (fourth row) and the anisotropic ZZP technique (fifth row).

with respect to the one yielded by the anisotropic ZZ procedure, as confirmed by the maximum aspect ratio equal to 160.88.

As a last check, we merge SIMPATY algorithm with the procedure employed in [21], following [44,22]. This consists of a projection which emphasizes the density gradient yielding a sharper material-void pattern starting from the filtered density. As a consequence, [Algorithm 2](#) has to be modified by replacing the input ρ_h^{k+1} of function adapt with ρ_p^{k+1} , where

$$\rho_p^{k+1} = 0.5 \left(1 + \frac{\tanh(\beta(\rho_f(\rho_h^{k+1}) - 0.5)))}{\tanh(0.5\beta)} \right),$$

ρ_f being the filtered density in (5) and with β a parameter tuning sharpening features. We refer to this variant of SIMPATY as to ZZP algorithm. In practice we expect that ZZP converges in fewer iterations since ρ_p is sharp but smoother than ρ_h . The resulting anisotropic adapted mesh, for $\beta = 20$, is shown in [Fig. 4](#), fifth row, and it consists of 2819 triangles with maximum aspect ratio equal to 75.34. The reduced number of elements and aspect ratio confirm the effectiveness of the projection step.

Table 1
CLC test case: compliance associated with different adapted meshes.

	AM	ZZ	ZZP
Isotropic	9.020(14)	9.060(23)	10.195(6)
Anisotropic	9.673(9)	8.852(18)	9.236(9)

Overall, all the four meshes in [Fig. 4](#) are fully comparable with the optimal-design structure provided in Fig. 18(3) in [23], where 24,576 structured triangles are employed.

[Table 1](#) provides the parameter design of interest, i.e., the compliance computed on the truncated mesh with unit density everywhere. The data refer to the three adaptive algorithms, i.e., the FreeFem++ function adaptmesh (first column), the plain SIMPATY algorithm (ZZ) (second column), and its variant with projection (ZZP) (third column), for both the isotropic (first row) and the anisotropic (second row) cases. In brackets, we furnish the number of iterations required to converge.

The minimum possible compliance is the one associated with the full-material structure and it is equal to 6.611. In this respect, the best compliance is achieved by the anisotropic ZZ approach, while the least performing structure is the one predicted by the isotropic ZZ method. The number of iterations is minimized by the ZZP algorithm, although also in the other cases the convergence is quite fast, compared, for instance, with Fig. 17 in [23].

4.2. Bottom Load Short Cantilever (BLSC)

In this section, we perform a more quantitative assessment by focusing on properties of relevance in an engineering setting. In particular, we cast the Bottom Load Short Cantilever (BLSC) test case in [45] in our framework by replacing the pointwise loads with a distributed traction, taking into account the thickness of the structure in the computation of the compliance and under a plane-stress assumption.

The design domain is $\Omega = (0, 1)^2$ for a thickness $t = 0.01$, and we choose in model (1) $\Gamma_D = \{(x, y) : x = 0, 0 \leq y \leq 1\}$, $\Gamma_N = \{(x, y) : x = 1, 0 \leq y \leq w\}$, with $w = 0.1$, $\Gamma_F = \partial\Omega \setminus (\Gamma_D \cup \Gamma_N)$, $\mathbf{f} = (0, -5.8 \cdot 10^4 / (wt))^T$ (see [Fig. 5](#)). The material considered is one of the most popular in structural mechanics, i.e., ASTM A-36 steel, characterized by $E = 2.11 \cdot 10^{11}$, $\nu = 0.29$ and by a yield strength $\sigma_y = 2.2 \cdot 10^8$. We set $p = 3$, while the SIMPATY input parameters are chosen as $CTOL = 10^{-2}$, $MTOL = 0.35$, $kmax = 30$, $\rho_{min} = 10^{-2}$, the initial mesh $\mathcal{T}_h^{(0)}$ is an $n \times n$ structured grid, for $n = 20, 40$ and 100 , and $\alpha = 0.5$. Finally, parameter nk is set to 20 at every iteration except for the first one where nk = 200. [Figs. 6–10](#) collect the results of the outputs provided by SIMPATY algorithm for $n = 20$ and 40 and by resorting to the adaptive procedures identified by the flags `method = "ZZ"` and `method = "AM"`. [Figs. 6](#) shows the material distribution. The employed

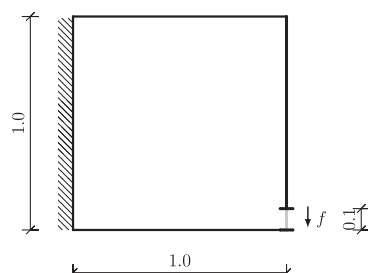


Fig. 5. BLSC test case: geometry and load.

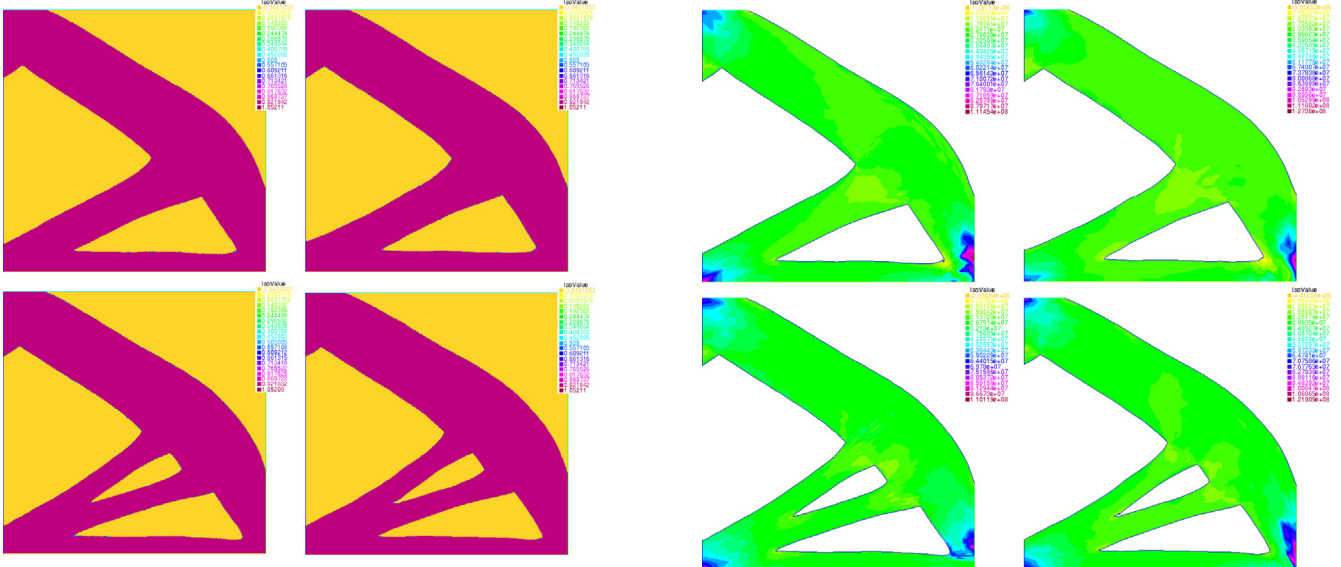


Fig. 6. BLSC test case: optimal density obtained for `method = "ZZ"` (left) and `method = "AM"` (right) with a 20×20 (top) and 40×40 (bottom) initial mesh.

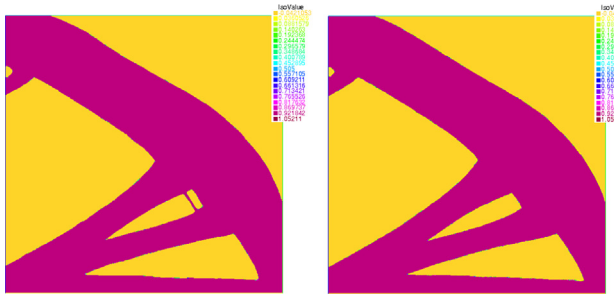


Fig. 7. BLSC test case: optimal density obtained for `method = "ZZ"` (left) and `method = "AM"` (right) with a 100×100 initial mesh.

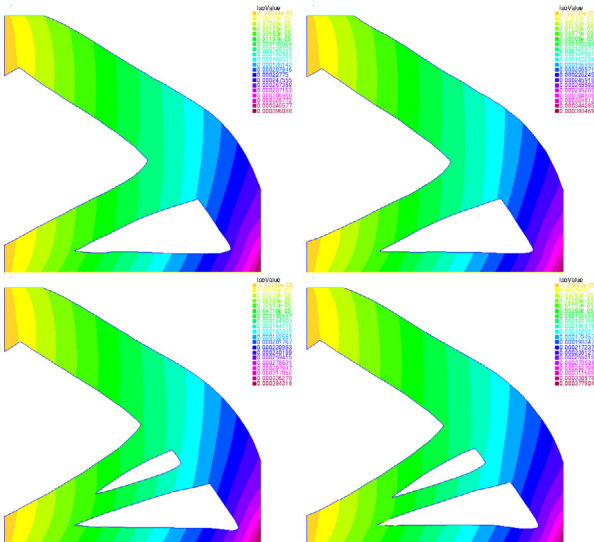


Fig. 8. BLSC test case: displacement on the final mesh obtained for `method = "ZZ"` (left) and `method = "AM"` (right) with a 20×20 (top) and 40×40 (bottom) initial mesh.

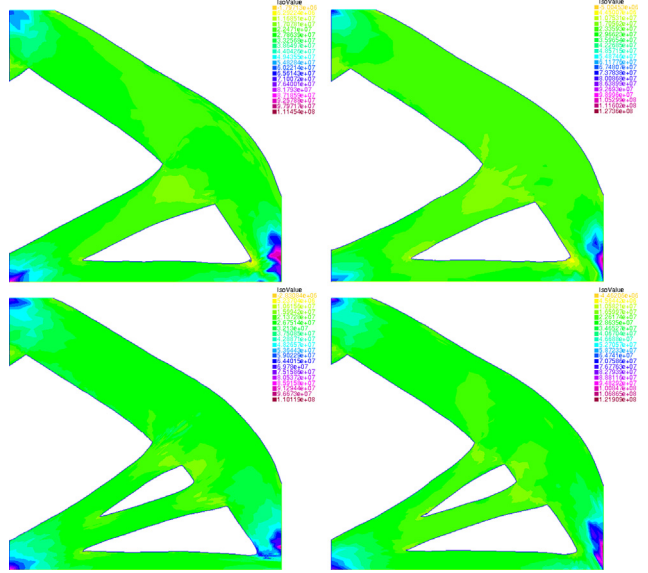


Fig. 9. BLSC test case: von Mises stress on the final mesh obtained for `method = "ZZ"` (left) and `method = "AM"` (right) with a 20×20 (top) and 40×40 (bottom) initial mesh.

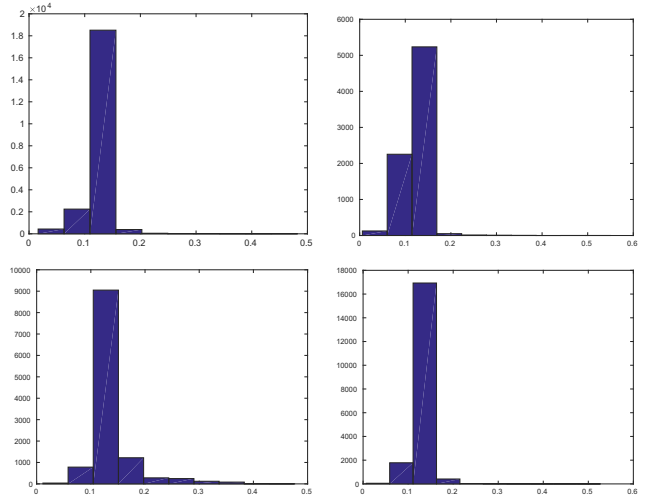


Fig. 10. BLSC test case: frequency distribution of `sf` at the nodes of the final mesh on 10 bins obtained for `method = "ZZ"` (left) and `method = "AM"` (right) with a 20×20 (top) and 40×40 (bottom) initial mesh.

adaptive strategy marginally affects the final structure, whereas the initial grid plays an important role. A finer grid seems to favour the generation of a more complex topology, as confirmed also by Fig. 7, where n is set to 100. The optimized structure more similar to the one in Fig. 32 (a) of [45] is obtained starting from the coarsest mesh ($n = 20$). Nevertheless, we highlight that the procedure adopted in [45] is different, since the authors apply SIMP with the OC (Optimality Criteria) method [46] on a fixed 100×100 quadrilateral mesh along with a filtering technique.

The absolute value of the structure displacement \mathbf{u}_h in Fig. 8 confirms that the stiffest structures are associated with the most complex ones, on noting that lower values imply a stiffer behaviour.

The von Mises stress, $\text{vM} = [\sigma_{11}^2 + \sigma_{22}^2 - \sigma_{11}\sigma_{22} + 3\sigma_{12}^2]^{1/2}$, is displayed in Fig. 9, with σ_{ij} the ij component of the stress tensor σ . Accordingly to Fig. 32(c) in [45], the highly stressed portions

of the structure are the clamped corners together with the loaded section. Additionally, we remark that the most complex structures allow us to alleviate the stress distribution especially on the clamped boundaries, even though no explicit constraint has been enforced on the stress.

Finally, Fig. 10 provides the frequency distribution of the safety factor, $sF = vM/\sigma_y$, which measures the resistance of the structure to the loads and, according to the von Mises yield criterion, should always satisfy $sF \leq 1$. A strong lumping of the bins characterizes all of the four panels, highlighting that all the points of the structure essentially work to the same extent.

The quantities shown in the last three figures, as well as the values in the following tables, have been computed on the final truncated mesh. Tables 2 and 3 gather more quantitative information related to the two adaptive procedures, “ZZ” and “AM”, for the two coarsest initial meshes. Figures are organized as follows: the first three rows refer to the output of SIMPATY algorithm, i.e., the number, #it, of iterations to converge, the cardinality, $\#\mathcal{T}_h$, of the final adapted mesh, and the maximum aspect ratio, $S_{K,\max} = \max_{K \in \mathcal{T}_h} S_K$; the next rows track five quantities of engineering relevance, namely, the compliance $C_t = t \int_{\Gamma_N} \mathbf{f} \cdot \mathbf{u}_h d\gamma$ taking into account the thickness of the cantilever, the maximum von Mises stress, vM_{\max} , at the mesh nodes, the maximum safety factor, $sF_{\max} = vM_{\max}/\sigma_y$, the average, avg(sF), and the standard deviation, std(sF), of the safety factor computed by a volume integral over the truncated domain.

A comparison between the two tables emphasizes that no remarkable difference can be appreciated between the quantities of interest. The structure is always working under safety conditions, the maximum safety factor being far from one. Moreover, the average value of sF, about one third of sF_{\max} , points out that few parts of the structure are highly stressed. The low value of the standard deviation confirms that the von Mises stress is almost uniform throughout the cantilever. It appears that the “ZZ” procedure delivers safer structures due to the lower values of sF_{\max} . Finally, a cross comparison of Tables 2 and 3 with Table 10 in [45] shows that there is a general agreement, despite the modeling differences between the two cases.

Table 2
BLSC test case: quantitative assessment for method = “ZZ”.

	ZZ 20 × 20	ZZ 40 × 40
#it	10	12
$\#\mathcal{T}_h$	19150	10337
$S_{K,\max}$	884.74	282.17
C_t	24.7314	24.8731
vM_{\max}	$1.06 \cdot 10^8$	$1.05 \cdot 10^8$
sF_{\max}	0.4821	0.4761
avg(sF)	0.1393	0.1418
std(sF)	$3.83 \cdot 10^{-2}$	$3.33 \cdot 10^{-2}$

Table 3
BLSC test case: quantitative assessment for method = “AM”.

	AM 20 × 20	AM 40 × 40
#it	15	23
$\#\mathcal{T}_h$	6710	16940
$S_{K,\max}$	150.02	587.94
C_t	22.2546	26.9122
vM_{\max}	$1.21 \cdot 10^8$	$1.16 \cdot 10^8$
sF_{\max}	0.5503	0.5268
avg(sF)	0.1312	0.1455
std(sF)	$3.67 \cdot 10^{-2}$	$3.84 \cdot 10^{-2}$

4.3. Michell structure

We now consider another standard benchmark, known as Michell truss, whose analytical solution was studied in [47]. The design domain is $\Omega = (0, 5.5) \times (0, 4)$ without the circle of radius 1 centered at $(1.5, 2)$, for a thickness $t = 0.05$. We choose in model (1) $\Gamma_D = \{(x, y) : (x - 1.5)^2 + (y - 2)^2 = 1\}$, $\Gamma_N = \{(x, y) : x = 5.5, |y - 2| \leq w/2\}$, with $w = 0.1$, $\Gamma_F = \partial\Omega \setminus (\Gamma_D \cup \Gamma_N)$, $\mathbf{f} = (0, -1/(wt))^T$ (see Fig. 11). The material parameters are set to $E = 1$, $\nu = 0.29$. We set $p = 3$, while the SIMPATY input parameters are chosen as $CTOL = 10^{-2}$, $MTOL = 0.35$, $kmax = 30$, $\rho_{min} = 10^{-2}$, the initial mesh $\mathcal{T}_h^{(0)}$ is isotropic with 60 edges on the rectangle sides as well as on the boundary of the circle. The variant ZZP is adopted, for two choices of the volume fraction, i.e., $\alpha = 0.4$ and $\alpha = 0.2$, respectively, with the common values $\tau = 1/38$ in the Helmholtz filter, and $\beta = 20$ for the projection. Finally, parameter nk is set to 50 at every iteration except for the first one where nk = 200. The resulting adapted mesh delivered by SIMPATY is displayed in Fig. 12, and is obtained by first applying the same truncation procedure used in the CLC test case, and then by uniformly splitting each triangle in four subtriangles. As can be noticed, the optimal layout is a continuum structure rather than a Michell truss. This was also observed in [18, Section 4.3.1.1], and justified by the fact

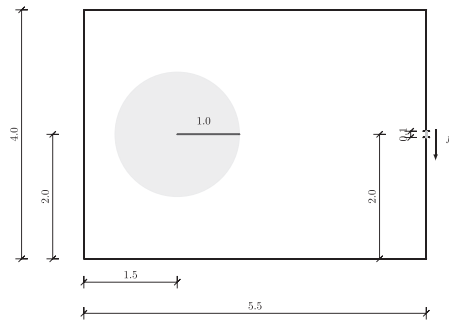


Fig. 11. Michell test case: geometry and load.

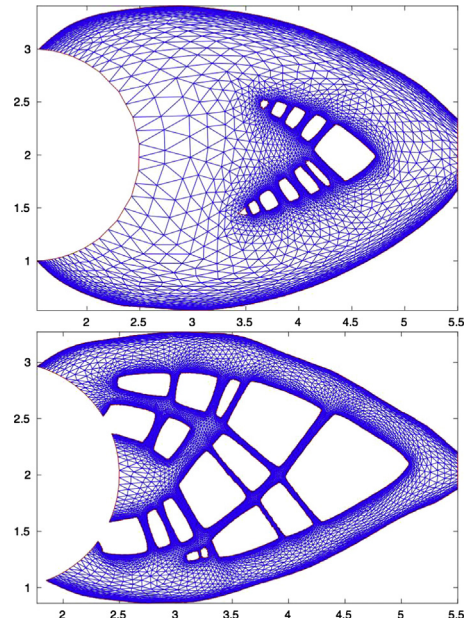


Fig. 12. Michell test case: adapted mesh $\mathcal{T}_h^{(13)}$ ($\alpha = 0.4$, top) and $\mathcal{T}_h^{(7)}$ ($\alpha = 0.2$, bottom).

that continuum topology optimization is a more general approach than the truss topology optimization method, and may or may not result in truss-like structures. Actually, configurations more similar to those studied in [47] can be observed as the volume fraction gets smaller and smaller (see Fig. 12, bottom).

5. Free shaping with SIMPATY

In this section, we finally move towards a free-form design by considering structural configurations where SIMPATY algorithm emphasizes its actual power.

5.1. Central Load L-shaped (CLL) lamina

This test case models the L-shaped lamina in Fig. 13 where the design domain is $\Omega = (0, 2.5)^2 \setminus [1, 2.5]^2$. The material properties in (1) are $E = 10^3$, $v = 1/3$, while the load is $\mathbf{f} = (0, -40)^T$, and the boundary data are $\Gamma_D = \{(x, y) : 0 \leq x \leq 1, y = 2.5\}$, $\Gamma_N = \{(x, y) : x = 2.5, 0.45 \leq y \leq 0.55\}$, $\Gamma_F = \partial\Omega \setminus (\Gamma_D \cup \Gamma_N)$.

Concerning the SIMP algorithm, we choose $p = 3$. Algorithm 2 is run with the input parameters $CTOL = 10^{-2}$, $MTOL = 0.5$, $kmax = 30$, $\rho_{min} = 10^{-2}$, $\mathcal{T}_h^{(0)}$ consisting of 512 elements and $\alpha = 0.5$.

For this configuration, we compare the plain SIMPATY algorithm (ZZ) with the variant ZZP, and a new approach (denoted by ZZG) based on a gradual variation of the SIMP exponent p as a function of the iteration number, k , according to the law $p = 3 - \exp(-k/2)$. A similar idea is adopted in [48] to avoid early convergence to a local minimum. In particular, the author increases the value of p every 20 iterations of the optimization algorithm, without any mesh adaptation.

Both the isotropic and anisotropic mesh adaptations are considered. Table 4 gathers the results of this comparison in terms of compliance and number of iterations demanded by SIMPATY to converge. The anisotropic approaches, ZZ and ZZG, perform comparably both in terms of compliance and convergence speed, whereas ZZP reduces the number of iterations and delivers a smaller compliance. In terms of number of elements, as expected, the anisotropic approach always outperforms the isotropic version as shown in Table 5. In particular, the gain in terms of mesh cardinality is about 3.6, 2.7 and 5.5 for the plain ZZ, the ZZP and the ZZG strategy, respectively.

Fig. 14 collects the adapted meshes generated by ZZ and the two variants ZZP and ZZG. The shape predicted by the three procedures is different despite preserving the external frame. It is remarkable the curved shape of the bottom-left boundary of the lamina, which represents a relevant feature with a view to a free-form design. This property is a *free lunch* of the proposed technique in contrast

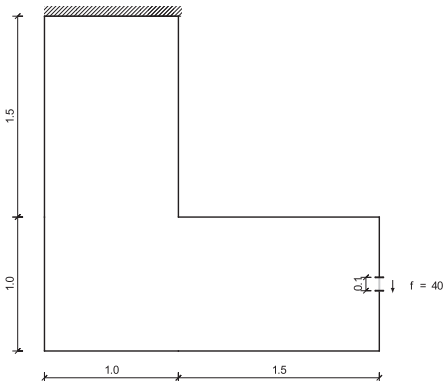


Fig. 13. CLL lamina test case: geometry and load.

Table 4

CLL lamina test case: compliance (number of iterations) associated with different adaptation strategies.

	ZZ	ZZP	ZZG
isotropic	2.1414(21)	2.0315(15)	2.3271(17)
anisotropic	2.2221(15)	1.9071(11)	2.1868(18)

Table 5

CLL lamina test case: number of elements associated with different adaptation strategies.

	ZZ	ZZP	ZZG
Isotropic	19896	8864	33737
Anisotropic	5544	3276	6125

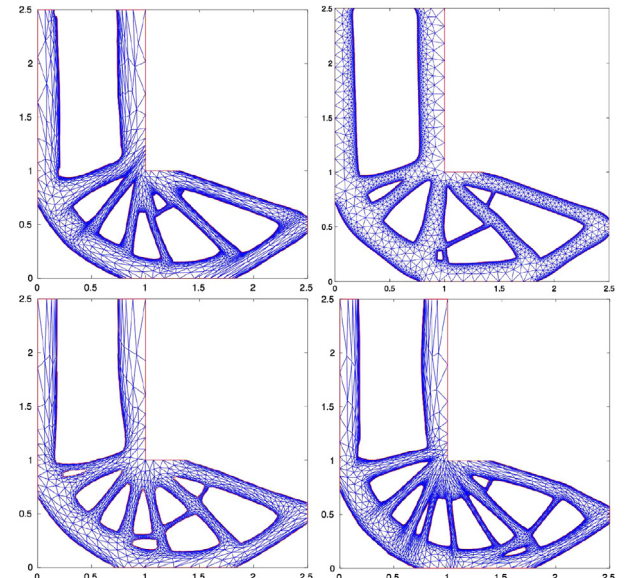


Fig. 14. CLL lamina test case: adapted mesh obtained with the anisotropic (top-left) and the isotropic (top-right) ZZ estimator, the anisotropic ZZP (bottom-left) and ZZG (bottom-right) estimator.

to what is usually available in the pertinent literature (see, e.g., [23,24]).

Finally, we carry out a cross-comparison among the three anisotropic approaches in terms of CPU time¹ and performance. Table 6 gathers the time (in seconds) required by the optimization (calls to IPOPT) and the mesh adaptation (computation of the metric and mesh generation), as well as the total time, which accounts also for setup and output operations. For all methods, most of the time is spent in the optimization phase, with a discrepancy of about 20X for the ZZ procedure.

Concerning the check on performance (see Fig. 15), we select the compliance as reference quantity, following [23]. The trend characterizing the ZZ and ZZP approaches is similar. After an initial spike, just after the global minimum value associated with the full structure, the compliance exhibits a piecewise decreasing pattern, marked by the mesh adaptation steps. This behavior is similar to what shown in [23]. The ZZG procedure shows a less regular trend, due to the further update of the penalty exponent p . It seems that the best overall performance is provided by ZZP.

¹ The computations have been run on a GenuineIntel Pentium(R) Dual-Core CPU E6300 2.80 GHz 4 GB RAM desktop computer.

Table 6

CLL lamina test case: CPU time associated with different adaptation strategies.

	ZZ	ZZP	ZZG
Optimization	505.59	320	293.35
Adaptation	27.13	16.22	28.34
Total	536.59	338.51	325.77

5.2. Design of an MBB beam

We exploit SIMPATY algorithm to devise an innovative shape for a bridge-like structure thanks to the potentialities offered by an anisotropic adaptive procedure.

The design domain is $\Omega = (0, 6) \times (0, 1)$. The boundary $\partial\Omega$ is subdivided into $\Gamma_D = \{(x, y) : 5.94 \leq x \leq 6, y = 0\}$, $\Gamma_R = \{(x, y) : 0 \leq x \leq 0.06, y = 0\}$, $\Gamma_N = \{(x, y) : 2.9 \leq x \leq 3.1, y = 0\}$, $\Gamma_F = \partial\Omega \setminus (\Gamma_D \cup \Gamma_R \cup \Gamma_N)$, where Γ_R represents the roller constraint $u_2 = 0$ (see Fig. 16 for a sketch). The load in (1) coincides with a vertical downward traction of magnitude 100, applied to either the top or the bottom edge of Ω (see Fig. 16), while the material properties are $E = 10^3$ and $v = 1/3$.

We confine the choice of the algorithm to the basic anisotropic ZZ procedure. In particular, to contain the branching feature of SIMPATY, which is particularly evident for this configuration, we pick as initial guess, ρ_h^0 , for the density, the output of five runs of twenty iterations of IPOPT alternated by the Helmholtz filter with $\tau = 1/30$, on a fixed grid $\mathcal{T}_h^{(0)}$ consisting of 5229 elements.

To investigate the free-shaping capability of SIMPATY procedure, we perform two bunches of simulations, by changing the load application area (top/bottom) together with the volume fraction α , chosen equal to 0.4, 0.5 and 0.6. The remaining input parameters are set to CTOL = $5 \cdot 10^{-2}$, MTOL = 0.65, kmax = 30 and $\rho_{\min} = 10^{-2}$.

Fig. 17 collects the structures corresponding to the bottom load, showing the final adapted mesh superposed to the density distribution. All the three configurations are not symmetric due to the different anchorage conditions applied to the bottom ends of Ω . As the volume fraction increases, we observe a thickening of the horizontal top and bottom portions of the structure together with an increasing number of secondary beams. We remark also the presence of a central vertical beam for the largest volume fraction. From Table 7, we infer that higher volume fractions require coarser grids and, as expected, lead to a less compliant structure. In Fig. 18, we gather the combined density/adapted mesh configuration when the load is applied on top. We highlight the more straightness of the final structure compared with the rounded forms in Fig. 17. In particular, the MBB beam associated with $\alpha = 0.4$ exhibits the least free-form features. As shown in Table 8, the compliance reduces as the volume fraction increases, while a significant reduction in the mesh cardinality occurs compared with the bottom load case.

We approach now the same test case by exploiting the procedure usually adopted in the literature according to which only half of the domain is simulated [46,45]. The intrinsic limit of this approach is that the actual fixed support is replaced by a roller, this leading to an under-constrained configuration. We consider the left half of the beam and enforce a symmetric boundary condition along the side $\{(x, y) : x = 3, 0 \leq y \leq 1\}$, i.e., $u_1 = 0$. We apply SIMPATY algorithm for both the bottom/top loads, for $\alpha = 0.5$ and by using the same values for all the other parameters, except for τ which switches between 1/10 and 1/30.

Figs. 19 and 20 show the resulting half MBB beams. By increasing τ the branching is less evident due to the stronger diffusivity of the Helmholtz filter. Moreover, the straightness and roundedness of the beam associated with the top and bottom load, respectively are maintained as in the full-geometry approach, although the micro structure is somewhat different.

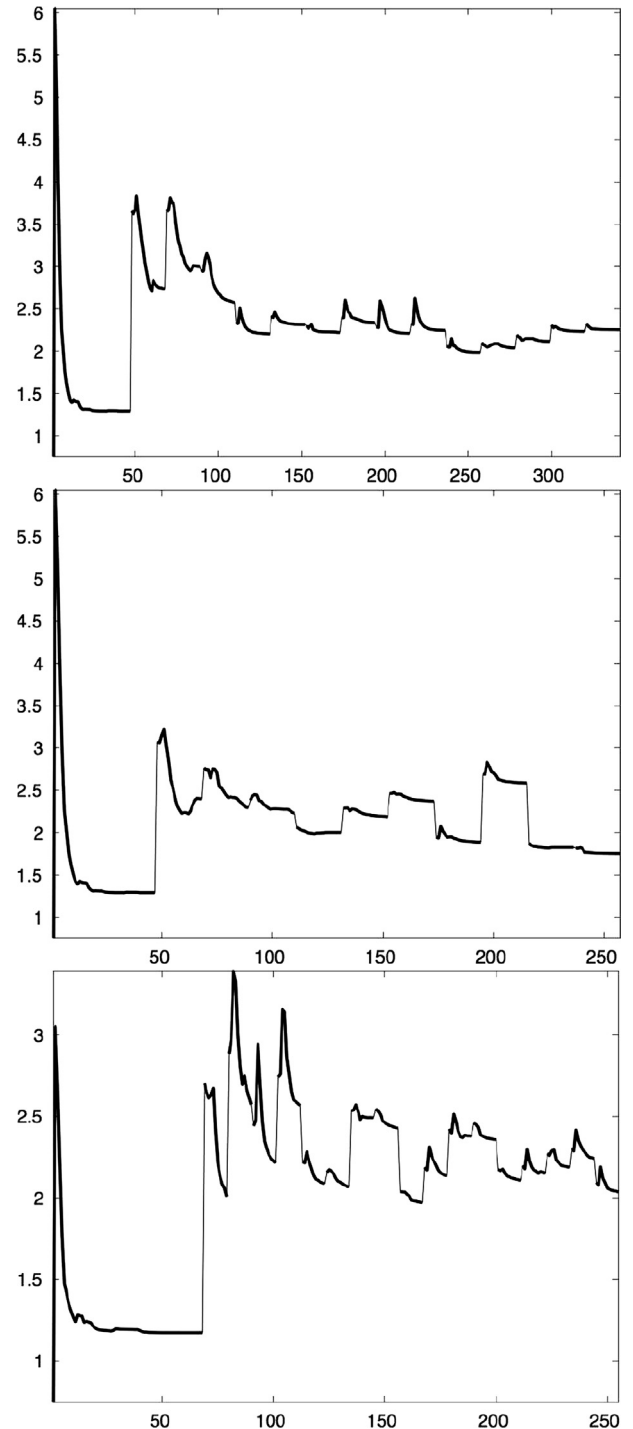


Fig. 15. CLL lamina test case: compliance history for the ZZ (top), ZZP (center) and ZZG (bottom) estimator.

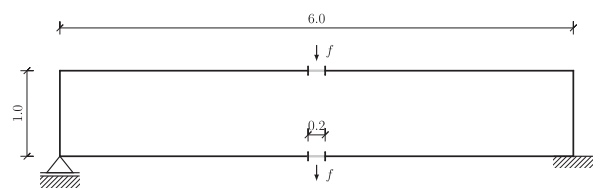


Fig. 16. MBB beam test case: geometry and load.

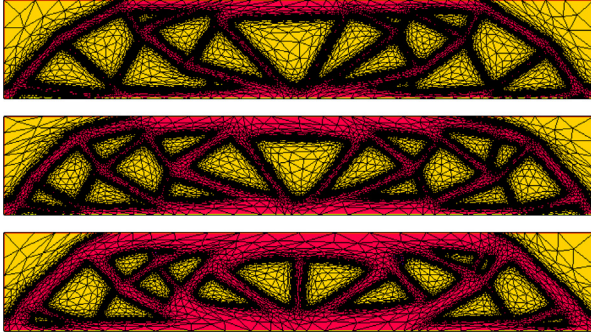


Fig. 17. MBB beam test case, bottom load: $\alpha = 0.4$ (top), $\alpha = 0.5$ (center), $\alpha = 0.6$ (bottom).

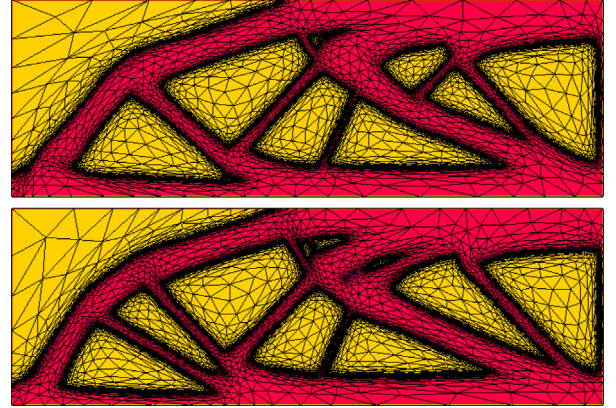


Fig. 19. Half MBB beam test case, bottom load: $\tau = 1/10$ (top), $\tau = 1/30$ (bottom).

Table 7
MBB beam test case, bottom load: number of iterations, cardinality and compliance for different volume fractions.

	$\alpha = 0.4$	$\alpha = 0.5$	$\alpha = 0.6$
#it	14	12	12
$\#\mathcal{T}_h$	30224	22952	12590
c	36.5774	21.0502	14.3752

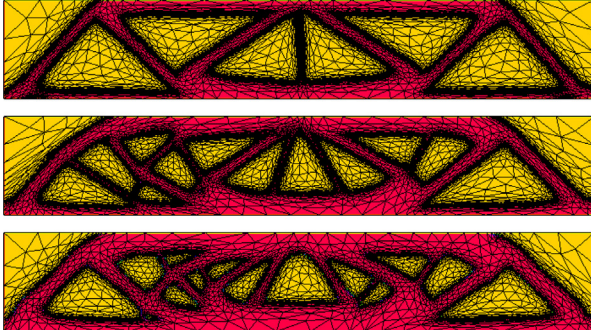


Fig. 18. MBB beam test case, top load: $\alpha = 0.4$ (top), $\alpha = 0.5$ (center), $\alpha = 0.6$ (bottom).

Table 8
MBB beam test case, top load: number of iterations, cardinality and compliance for different volume fractions.

	$\alpha = 0.4$	$\alpha = 0.5$	$\alpha = 0.6$
#it	10	13	9
$\#\mathcal{T}_h$	14976	12006	7819
c	34.8155	33.2496	24.5489

5.3. Additive manufacturing for a satellite component

We move now towards a more realistic application, i.e., the topology optimization of satellite components as, for example, an antenna bracket. For example, to save on the cost of the launch, orbital maneuvers operation, and satellite qualification development, each component should be designed to be as much small-mass as possible. Launch costs per kilogram of mass vary from several thousand of Euros to tens of thousand of Euros, depending on the orbit altitude in case of Earth satellite, and even much higher for interplanetary missions (see [49]).

To model the bracket, we consider the simplified geometry in Fig. 21, made by two rectangles with constant cross-section, glued by a circular joint. In particular, we select $H = L_1 = 1, L_2 = R = 2$

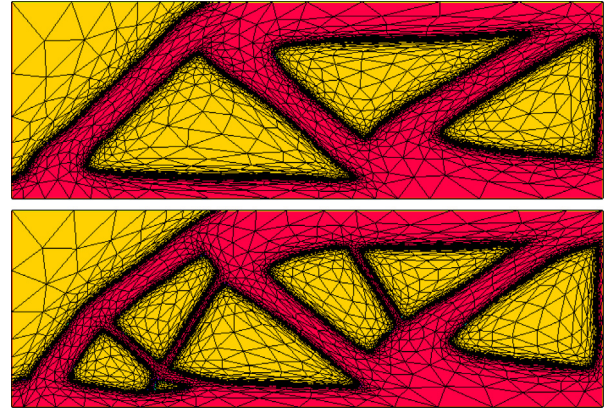


Fig. 20. Half MBB beam test case, top load: $\tau = 1/10$ (top), $\tau = 1/30$ (bottom).

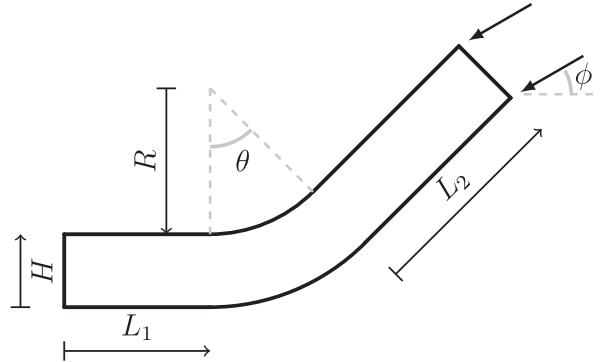


Fig. 21. Antenna bracket test case: geometry and load.

and $\theta = \pi/3$. The material properties are $E = 10^3$, $v = 1/3$, while the load has a uniform magnitude 100, makes an angle ϕ to the horizontal direction, and is applied on two outer portions of width 0.1 each. The bracket is fixed at the left boundary, the remaining portion of $\partial\Omega$ being traction-free. It is clearly understood that the analysis here provided is only qualitative.

The plain SIMPATY algorithm is applied with the input parameters $CTOL = 10^{-2}$, $MTOL = 0.45$, $kmax = 30$, $\rho_{min} = 10^{-2}$, an initial mesh consisting of 1712 triangles and $\alpha = 0.4$. We select three different values for the angle ϕ , namely, 0 (horizontal load), $\pi/3$ (load parallel the tilted rectangle) and $\pi/2$ (vertical load).

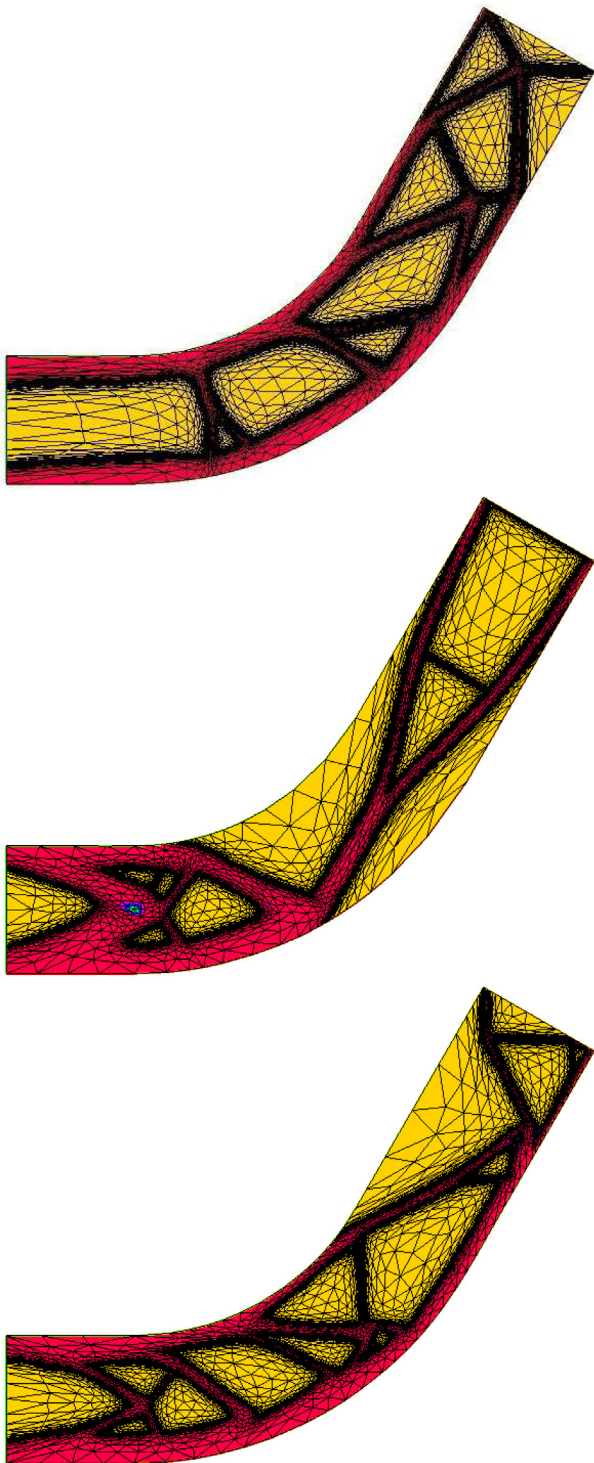


Fig. 22. Antenna bracket test case: $\phi = 0$ (top), $\phi = \pi/3$ (center), $\phi = \pi/2$ (bottom).

Fig. 22 collects the output of SIMPATY algorithm. The three layouts are quite different, and reflect the load direction. In particular, the top and the bottom ones are subjected to a bending moment which is counter-balanced by a lattice structure throughout the whole design domain. When the load is parallel to the structure, a compressive stress is dominant and channeled into a tuning fork connected to a cantilever in the bottom-left part of the bracket, as shown in the central panel.

Although the qualitative scope of our analysis, values in **Table 9** show that the least compliant structure is the one where $\phi = \pi/3$,

Table 9

Antenna bracket test case: number of elements and compliance for different load angles.

	$\phi = 0$	$\phi = \pi/3$	$\phi = \pi/2$
$\#\mathcal{T}_h$	14765	11119	11771
C	23.0882	4.3002	21.7114

due to the reduced bending deformation of the layout. We also observe a small sensitivity of the number of the mesh elements to the load angle.

6. Conclusions and future scenarios

SIMPATY algorithm turned out to be a reliable strategy both qualitatively and quantitatively. In particular, the verification on the standard SCBL benchmark has shown that engineering relevant quantities are correctly predicted, even with a considerable reduction of computational costs, and the structure works under safety conditions. Qualitatively, the optimized layouts exhibit impressive free-form features, such as the rounded contours in the CLL lamina and in the MBB beam test cases. Moreover, the anisotropic mesh adaptation allows us to get rid of the checkerboard phenomenon. This is also made possible by the employment of nodal design variables, the density being approximated via continuous piecewise linear finite elements, in contrast to a more standard piecewise constant discretization. Mesh dependency remains an issue, possibly due to the nonuniqueness of the solution to the optimization problem.

Concerning future developments, we are currently generalizing SIMPATY algorithm to a 3D setting. This will represent the subject of a forthcoming paper. Finally, we remark that, thanks to the recovery-based error estimator, depending only on the density and not on the target criteria, the approach proposed here can be applied in a straightforward way to the optimization of several quantities, other than the compliance, such as the fundamental frequency of a structure. Another topic of potential interest is represented by a multi-objective framework, for instance, by including the thermal analysis into the current structural setting.

Acknowledgements

This work has been developed within the activities of MetaMat-Lab of Politecnico di Milano.

The first and second authors developed part of this research under the INdAM-GNCS2017 Project *Metodi Numerici Avanzati Combinati con Tecniche di Riduzione Computazionale per PDEs Parametrizzate e Applicazioni*, and thank Thales Alenia Space Italia for promoting this subject of investigation.

SIMPATY algorithm is the subject of an Italian patent application (No. 102016000118131), filed on November 22, 2016 and of an International patent application PCT (No. PCT/IB2017/057323).

Finally, all the authors warmly thank Nicola Ferro for his contribution on some test cases.

References

- [1] Alaimo MCG, Auricchio F, Zingales M. Multi-objective optimization of nitinol stent design. *Med Eng Phys* 2017;47:13–24.
- [2] Collet MBM, Duysinx P. Topology optimization for minimum weight with compliance and simplified nominal stress constraints for fatigue resistance. *Struct Multidisc Optim* 2017;55(3):839–55.
- [3] Bruggi M, Cinquini C. Topology optimization for thermal insulation: an application to building engineering. *Eng Optim* 2011;43(11):1223–42.
- [4] Zargham RRS, Ward TA, Badruddin I. Topology optimization: a review for structural designs under vibration problems. *Struct Multidisc Optim* 2016;53(6):1157–77.

- [5] Eschenauer HA, Olhoff N. Topology optimization of continuum structures: a review. *Appl Mech Rev* 2001;54(4):331–90.
- [6] Bendsøe MP, Kikuchi N. Generating optimal topologies in structural design using a homogenization method. *Comput Methods Appl Mech Eng* 1988;71(2):197–224.
- [7] Bendsøe MP, Sigmund O. Topology optimization: theory, methods and applications. Berlin Heidelberg: Springer-Verlag; 2003.
- [8] Sigmund O, Maute K. Topology optimization approaches. A comparative review. *Struct Multidisc Optim* 2013;48(6):1031–55.
- [9] Deaton JD, Grandhi RV. A survey of structural and multidisciplinary continuum topology optimization: post 2000. *Struct Multidisc Optim* 2014;49:1–38.
- [10] Rozvany GIN. A critical review of established methods of structural topology optimization. *Struct Multidisc Optim* 2009;37:217–37.
- [11] Allaire G, Jouve F, Toader A. Structural optimization using sensitivity analysis and level set-method. *J Comput Phys* 2004;194:363–93.
- [12] Wang XWM, Guo D. A level set method for structural topology optimization. *Comput Methods Appl Mech Eng* 2003;192(1-2):227–46.
- [13] Sokolowski J, Zochowski A. On the topological derivative in shape optimization. *SIAM J Control Opt* 1999;37:1251–72.
- [14] Dede L, Borden MJ, Hughes TJR. Isogeometric analysis for topology optimization with a phase field model. *Arch Comput Methods Eng* 2012;19:427–65.
- [15] Bourdin B, Chambolle A. Design-dependent loads in topology optimization. *ESAIM Control Optim Calc Var* 2003;9:19–48.
- [16] Xie Y, Steven G. A simple evolutionary procedure for structural optimization. *Comput Struct* 1993;49:885–96.
- [17] Allaire FJG, Maillot H. Topology optimization for minimum stress design with the homogenization method. *Struct Multidisc Optim* 2004;28:87–98.
- [18] Liang Q. Performance-based optimization of structures, theory and applications. London: Spon Press; 2005.
- [19] Diaz A, Sigmund O. Checkerboard patterns in layout optimization. *Struct Multidisc Optim* 1995;19:89–92.
- [20] Sigmund O, Petersson J. Numerical instabilities in topology optimization: a survey on procedures dealing with checkerboards, mesh-dependencies and local minima. *Struct Optim* 1998;16(1):68–75.
- [21] Lazarov BS, Sigmund O. Filters in topology optimization based on Helmholtz-type differential equations. *Int J Numer Methods Eng* 2011;86(6):765–81.
- [22] Sigmund O. Morphology-based black and white filters for topology optimization. *Struct Multidisc Optim* 2007;33:401–24.
- [23] Bruggi M, Verani M. A fully adaptive topology optimization algorithm with goal-oriented error control. *Comput Struct* 2011;89:1481–93.
- [24] Jensen KE. Solving stress and compliance constrained volume minimization using anisotropic mesh adaptation, the method of moving asymptotes and a global p-norm. *Struct Multidisc Optim* 2016;54(4):831–41.
- [25] Micheletti S, Perotto S. Anisotropic adaptation via a Zienkiewicz-Zhu error estimator for 2D elliptic problems. In: Kreiss G, Lötstedt P, Målqvist A, Neytcheva M, editors. Numerical mathematics and advanced applications. Berlin Heidelberg: Springer-Verlag; 2010. p. 645–53.
- [26] Farrell PE, Micheletti S, Perotto S. An anisotropic Zienkiewicz-Zhu type error estimator for 3D applications. *Int J Numer Methods Eng* 2011;85:671–92.
- [27] Farrell PE, Micheletti S, Perotto S. A recovery-based error estimator for anisotropic mesh adaptation in CFD. *Bol Soc Esp Matapl* 2010;50:115–38.
- [28] Micheletti S, Perotto S, Soli L. Ottimizzazione topologica adattativa per la fabbricazione stratificata additiva, Italian patent application No. 102016000118131, filed on November 22, 2016 (extended as Adaptive topology optimization for additive layer manufacturing, International patent application PCT No. PCT/IB2017/057323); 2017.
- [29] Gould PL. Introduction to linear elasticity. 2nd ed. New York: Springer; 1983.
- [30] Lions E, Magenes JL. Non-homogeneous boundary value problems and applications, vol. I. Berlin: Springer-Verlag; 1972.
- [31] Ciarlet PG. The finite element method for elliptic problems. Amsterdam: North-Holland; 1978.
- [32] IPOPT. Interior Point OPTimizer; 2017. <http://projects.coin-or.org/Iopt>.
- [33] Wächter A. An interior point algorithm for large-scale nonlinear optimization with applications in process engineering [Ph.D. thesis]. Carnegie Mellon University; 2002.
- [34] Dede L, Micheletti S, Perotto S. Anisotropic error control for environmental applications. *Appl Numer Math* 2008;58(9):1320–39.
- [35] Micheletti S, Perotto S. Output functional control for nonlinear equations driven by anisotropic mesh adaption: the Navier-Stokes equations. *SIAM J Sci Comput* 2008;30(6):2817–54.
- [36] Zienkiewicz OC, Zhu JZ. A simple error estimator and adaptive procedure for practical engineering analysis. *Int J Numer Meth Eng* 1987;24:337–57.
- [37] Zienkiewicz OC, Zhu JZ. The superconvergent patch recovery and a posteriori error estimates. I: The recovery technique. *Int J Numer Meth Eng* 1992;33:1331–64.
- [38] Zienkiewicz OC, Zhu JZ. The superconvergent patch recovery and a posteriori error estimates. II: Error estimates and adaptivity. *Int J Numer Meth Eng* 1992;33:1365–82.
- [39] Formaggia L, Perotto S. New anisotropic a priori error estimates. *Numer Math* 2001;89(4):641–67.
- [40] George P-L, Borouchaki H. Delaunay triangulation and meshing. Application to finite elements. Paris: Edition Hermès; 1998.
- [41] Micheletti S, Perotto S. The effect of anisotropic mesh adaptation on PDE-constrained optimal control problems. *SIAM J Control Optim* 2011;49(4):1793–828.
- [42] Micheletti S, Perotto S. Reliability and efficiency of an anisotropic Zienkiewicz-Zhu error estimator. *Comput Methods Appl Mech Eng* 2006;195(9):799–835.
- [43] Hecht F. New development in FreeFem++. *J Numer Math* 2012;20(3–4):251–65.
- [44] Guest JK, Prevost JH, Belytschko T. Achieving minimum length scale in topology optimization using nodal design variables and projection functions. *Int J Numer Methods Eng* 2004;61(2):238–54.
- [45] Valdez SI, Botello S, Ochoa MA, Marroquín JL, Cardoso V. Topology optimization benchmarks in 2D: results for minimum compliance and minimum volume in planar stress problems. *Arch Comput Methods Eng* 2017;24(4):803–39.
- [46] Sigmund O. A 99 line topology optimization code written in Matlab. *Struct Multidisc Optim* 2001;21:120–7.
- [47] Michell A. The limits of economy of material in frame-structures. *Philos Mag* 1904;8:589–97.
- [48] Lazarov BS. Topology optimization using multiscale finite element method for high-contrast media. In: Lirkov Ivan, Margenov Svetozar, Waśniewski Jerzy, et al., editors. Large-scale scientific computing, lecture notes in computer science. Berlin Heidelberg: Springer-Verlag; 2014. p. 339–46.
- [49] Amos J. SpaceX launches SES commercial TV satellite for Asia. BBC News; 2013.